Eruption of a Magnetic Flux Rope in a Comprehensive Radiative Magnetohydrodynamic Simulation of flare-productive active regions

Feng Chen,[1, 2, 3, 4] Matthias Rempel,[4] and Yuhong Fan[4]

[1]*School of Astronomy and Space Science, Nanjing University, Nanjing, 210023, China*
[2]*Key Laboratory for Modern Astronomy and Astrophysics (Nanjing University), Ministry of Education, Nanjing, 210023, China*
[3]*Laboratory for Atmospheric and Space Physics, University of Colorado, Boulder, 80303, USA*
[4]*High Altitude Observatory, National Center for Atmospheric Research, Boulder, 80307, USA*

ABSTRACT

Radiative magnetohydrodynamic simulation includes sufficiently realistic physics to allow for the synthesis of remote sensing observables that can be quantitatively compared with observations. We analyze the largest flare in a simulation of the emergence of large flare-productive active regions described by Chen et al. The flare is accompanied by a spectacular coronal mass ejection and reaches M2 class, as measured from synthetic soft X-ray flux. The eruption reproduces many key features of observed solar eruptions. A pre-existing magnetic flux rope is formed along the highly sheared polarity inversion line between a sunspot pair and is covered by an overlying multi-pole magnetic field. During the eruption, the progenitor flux rope actively reconnects with the canopy field and evolves to the large-scale multi-thermal flux rope that is observed in the corona. Meanwhile, the magnetic energy released via reconnection is channeled down to the lower atmosphere and gives rise to bright soft X-ray post-flare loops and flare ribbons that reproduce the morphology and dynamic evolution of observed flares. The model helps to shed light on questions of where and when the a flux rope may form and how the magnetic structures in an eruption are related to observable emission properties.

1. INTRODUCTION

A general picture of solar flares as a result of abrupt release of magnetic energy via reconnection has been well summarized by classical two-dimensional models (Priest & Forbes 2002; Shibata & Magara 2011). A three-dimensional standard flares model proposed by Aulanier et al. (2012) connects observed signatures of flares with the topological properties of the reconnected magnetic field. Since decades ago, flares and coronal mass ejections (CMEs) have been considered in a unified scenario of solar eruptions (e.g., Shibata et al. 1995). CME models pay more attention to the trigger of eruptions and propagation of the erupted magnetic structure (Forbes & Isenberg 1991; Antiochos et al. 1999; Lin & Forbes

2000; Chen & Shibata 2000; Moore et al. 2001; Török et al. 2004). The abundant modeling works on CMEs and their connection with observations in the past several decades have been comprehensively reviewed and discussed by Chen (2011); Janvier et al. (2015); Cheng et al. (2017); Green et al. (2018); Archontis & Syntelis (2019); Georgoulis et al. (2019).

Realistic models of solar eruptions that bring together the sophisticated energetic consideration of flaring plasma as in one-/two-dimensional models (Fisher et al. 1985; Kowalski et al. 2017) and the 3D geometry and magnetic topology similar to actual eruptions (e.g., Amari et al. 2003; Aulanier et al. 2010; Kusano et al. 2012; Wyper et al. 2017; Jiang et al. 2021) are immensely needed to bridge the gap between models and observations. With a focus on the evolution of an initially unstable eruption progenitor in the large-scale corona, some MHD models have taken into account a more realistic treatment of plasma thermodynamics (Jin

Corresponding author: Feng Chen
chenfeng@nju.edu.cn

et al. 2017; Downs et al. 2021; Fan 2022) and allowed model synthesized observables to be compared with observations. Cheung et al. (2019) reported a 3D radiative MHD simulation that accounts for optically thick radiative transport in the photosphere. Such treatment allows a more self-consistent description of flux emergence starting from the convective zone and meaningful synthesis of observables in the lower solar atmosphere.

With the same numerical method, Chen et al. (2022) simulated the evolution of flare-productive active regions by the emergence of active-region-scale flux bundles. Over a time period of 48 hours, more than one hundred flares that are larger than B-class occur spontaneously as an integral part of the emergence of active regions. Following the preceding paper that describes the general properties of the quiet Sun and active region evolution, we present in this paper an overview of the strongest and most spectacular flare event in the simulation. The simulation setup is briefly reviewed in Section 2. Section 3 shows the emission and magnetic properties of the event of interest. We compare the simulation results with observations in Section 4.

2. SIMULATION SETUP AND THE FLARE

The simulation is performed with the MURaM code (Rempel 2017), which accounts for the radiative transfer under local thermal equilibrium approximation and optically thin radiation and field-aligned thermal conduction in the transition region and corona. The simulation domain spans 196.608 Mm in the horizontal direction and 122.88 Mm in the vertical direction, which is resolved by 1024 and 1920 grid points, yielding resolutions of 192 and 64 km, respectively. The bottom boundary is placed at about 10 Mm beneath the photosphere, where flux bundles generated in a solar convective dynamo (Fan & Fang 2014) emerge into the domain as implemented by Chen et al. (2017). A detailed description of the simulation setup is presented in Chen et al. (2022). After an evolution of 48 hours solar time, the domain contains more than 10^{23} Mx unsigned magnetic flux and close to 10^{33} erg free magnetic energy, as well as complex shaped sunspots similar to flare productive active regions of the real Sun.

The event of interest, which is largest and arguably the most intriguing flare in the simulation, is initiated at $t \approx 27\,h42\,m$ and peaks at $t = 27\,42\,m\,20\,s$. The synthetic GOES flux of this flare reaches an absolute peak value of $2.7 \times 10^{-5}\mathrm{W\,m^{-2}}$ and a background deducted peak of $1.8 \times 10^{-5}\mathrm{W\,m^{-2}}$. About 4.5×10^{31} erg of magnetic energy is released during the event, a large portion of which contributes to the kinetic energy of an erupted flux rope that eventually develops into a CME. The CME makes

this flare an exceptional case in the entire simulation, as all the other eruptions that occur in the simulation are confined.

3. RESULTS

3.1. *Source Region of the Eruption*

The flare occurs in the bipole at the north edge (larger y) of the complex active region formed by the emerged flux bundles, as shown by the photospheric ling-of-sight magnetic field in Figure 1(a). Figure 1(b) shows a zoomed view of the sunspot pair, with the arrows showing the horizontal magnetic field[1]. It is clear that the horizontal magnetic field between the two spots is strongly sheared and apparently wraps around the negative polarity sunspot. To further illustrate the strong deviation of the magnetic field from the potential field, we evaluate the angle θ_p between the actual magnetic field and the potential field by

$$\theta_{\mathrm{p}} = \arccos\left(\frac{\mathbf{B} \cdot \mathbf{B_P}}{|\mathbf{B}||\mathbf{B_P}|}\right), \qquad (1)$$

where $\mathbf{B}$ is the magnetic vector on the surface of optical depth (τ) of unity, and the potential field B_p is calculated from the B_z in the same τ surface[2], with the condition of vanishing B_z at infinity and periodic side boundaries (for the entire domain). The angle is presented in Figure 1(c) with a color scale saturated at $90°$ and contour lines of $B_z = \pm 1500\,\mathrm{G}$ that outline the sunspots. The magnetic field inside the sunspots is close to a potential field. It is particularly interesting to note that spots are surrounded by a highly non-potential field, as indicated by angles near or larger than $90°$, while the region right in between the two spots is of smaller angles. This suggests a non-uniform distribution of shear along the PIL, whose implication will be discussed in combination with the observational properties of the flare.

We demonstrate in Figure 2 the presence of a magnetic flux rope before the eruption. The axis of the flux rope more or less follows the PIL with a toroidal field winding around. The magnetic field above the flux rope falls more in line with the potential field (directly connecting the sunspots, or namely, normal to the PIL), as they are located higher from the photosphere. One of the foot points of the flux rope is found at the right

---

[1] Arrows are only plotted in the region of $|B_z| \leq 2000\,\mathrm{G}$ to improve the visibility.

[2] This option mimics the effect in observations that measures the magnetic field in a tau surface instead of a geometrically horizontal layer. We have compared the results by using the magnetic field in a horizontal slice that corresponds to the photospheric height. The fact that the horizontal magnetic field is strongly sheared along the PIL and wraps the sunspots is not affected.
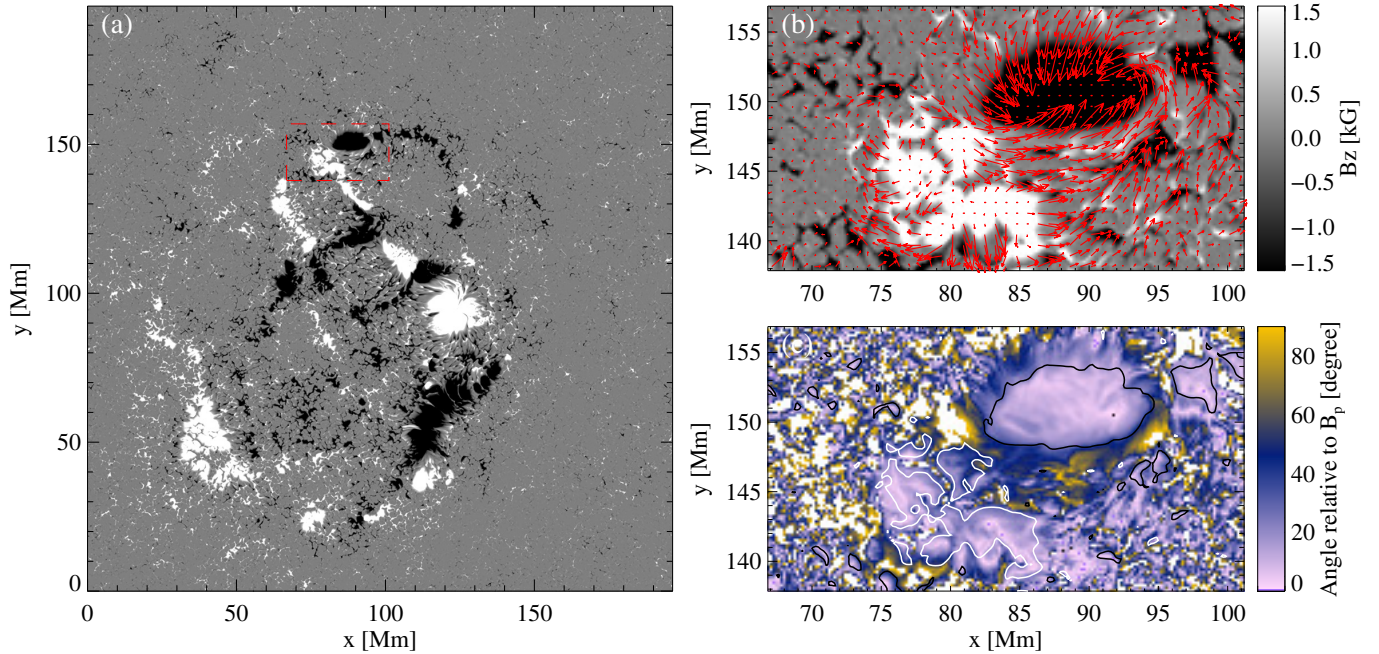
Figure 1. Magnetic field of the source region of the eruption. (a): Line-of-sight magnetic field (B_z) in the photosphere (surface of optical depth of unity). The red box indicates the source active region of the flare. (b): B_z in the source region. Arrows show the vector of the horizontal magnetic field. (c): Angles between the actual magnetic field (full vector) and the potential field in the photosphere.

(larger x) edge of the negative polarity spot, as can be inferred from the photospheric horizontal field. Figure 2(b) gives a view of the magnetic field along the PIL immediately beneath the photosphere. We note that the field lines shown are calculated from a different group of seed points. The sub-surface field lines are also strongly sheared along the PIL; however, they are seemingly less twisted than their counterpart above the photosphere. Therefore, the sub-surface magnetic field is more similar to sheared arcades. Figure 2(c) displays B_x in a $y-z$ plane that intersects the flux rope at $x=87$ Mm. B_x mostly presents the axial field of the flux rope, while the arrows clearly illustrate the twist. Chromospheric plasma is trapped in the dip of the flux rope, as shown in Figure 2 (d) & (f).

3.2. Observable Features of the Eruption

3.2.1. General Evolution of The Flux Rope Eruption

The emission measure (EM) is a key high-cadence output of the simulation (Rempel 2017; Chen et al. 2022) and serves as the primary tool for diagnosing plasma thermodynamics as done in observations. We present in Figure 3 the EMs integrated over three temperature ranges. This snapshot is 9 s after the GOES flux peak, with an animated version covering the full course of the eruption.

The animation shows that the very first signature of the eruption can be seen in the frame near

$t=27$ h, 41 m 30 in the low-temperature EM in panel (b) at $y\approx150$ Mm and in the high-temperature EM in panel (e) at $x\approx65$ Mm, which means that the eruption is initiated at one end of the flux rope, instead of the middle part of it. The asymmetric eruption quickly develops into a cone-like structure that expands and rotates while rising upward, as displayed by the middle-temperature EM in Figure 3(c). The mass load in the initial flux rope is mostly in chromospheric temperatures (10^4 K), as shown in Figure 2(d). However, the erupting flux rope is mostly magnificently seen transition-region and coronal temperatures, which indicate a significant heating of the trapped plasma during the eruption.

The high-temperature EM along the x-axis in panel (f) shows that the erupting flux rope encounters some canopy loops at $z\approx60$ Mm ($t\approx27$ h 43 m in the animation). The flux rope pushes them upward and evolves into a new structure by reconnection with the overlying magnetic field, as presented later in the paper. The location where reconnection occurs under the erupting flux rope is outlined in Figure 3(e) by a thin inclined thread of hot plasma (from $(x,z)=(100,10)$ Mm to $((x,z)=(50,60)$ Mm), which is roughly along the low edge of the cooler cone-like structure shown in panel (c). The brightest feature in the high-temperature EM is a series of post-flare loops found around $x\approx80$ Mm and $y=150$ Mm. These loops are the main emitter in the
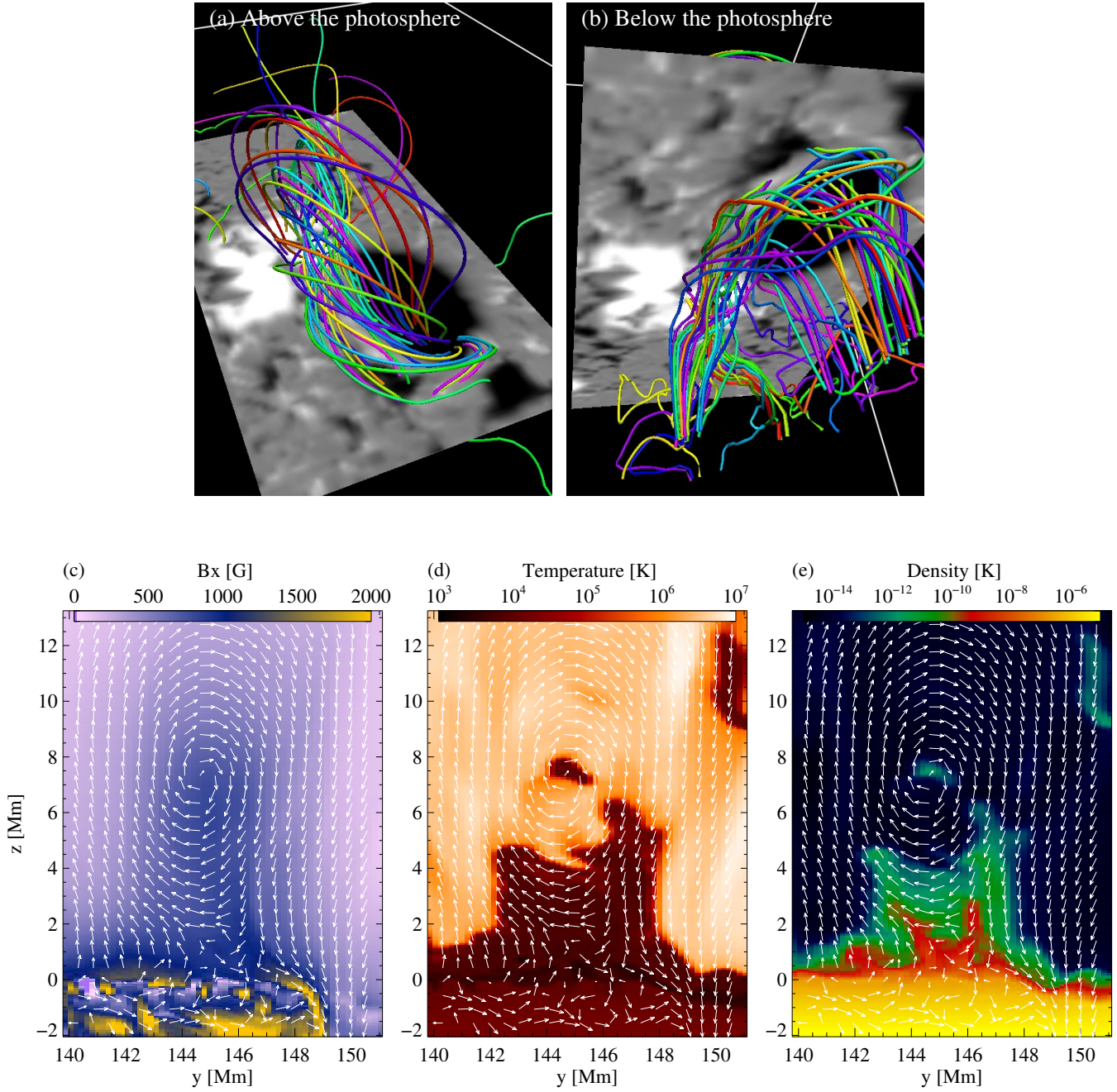
Figure 2. The magnetic flux rope along the photospheric polarity inversion line (PIL). (a): Magnetic field lines above the photosphere. The photosphere shown here is a horizontal layer with an average optical depth of unity. (b): Magnetic field beneath the photosphere. Field lines are calculated from seed points that are randomly distributed along the PIL and above/below the photosphere. Colors indicate different magnetic field lines. (c): B_x in a vertical cut ($y - z$ plane) at x=87 Mm. Arrows show the direction of the magnetic field in the plane (B_y and B_z). (d) & (f): Plasma temperature and density in the same vertical cut.
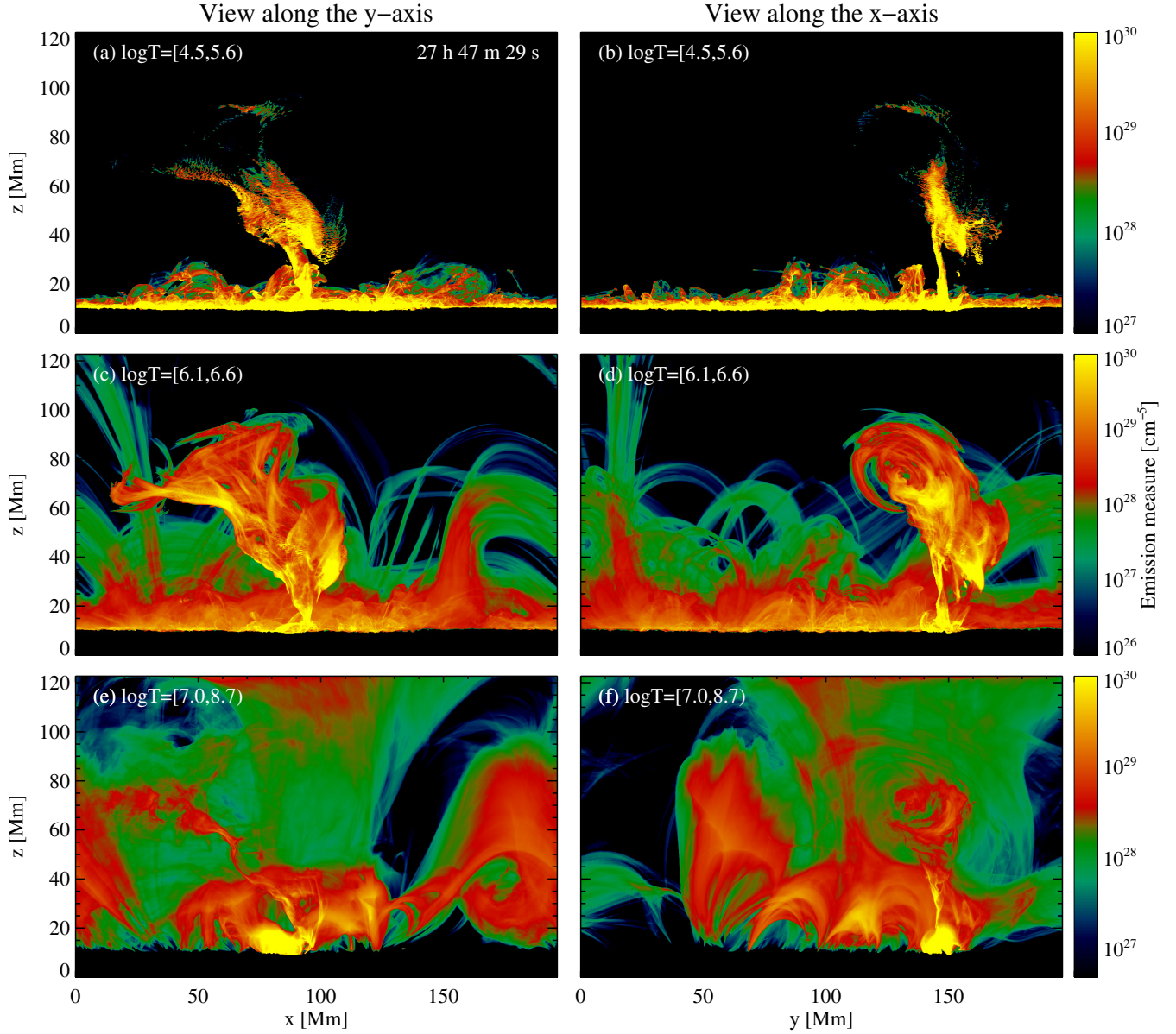
Figure 3. Emission measures in three temperature ranges. The left column shows a line-of-sight along the y-axis of the domain. The right column shows a view along the x-axis of the domain, corresponding to observations on the east limb of the Sun. The time stamp of this snapshot is 9 s after the flare peak. An animation that covers the dynamics evolution of about 40 min starting from about 20 min before the flare peak is available in the electronic version.
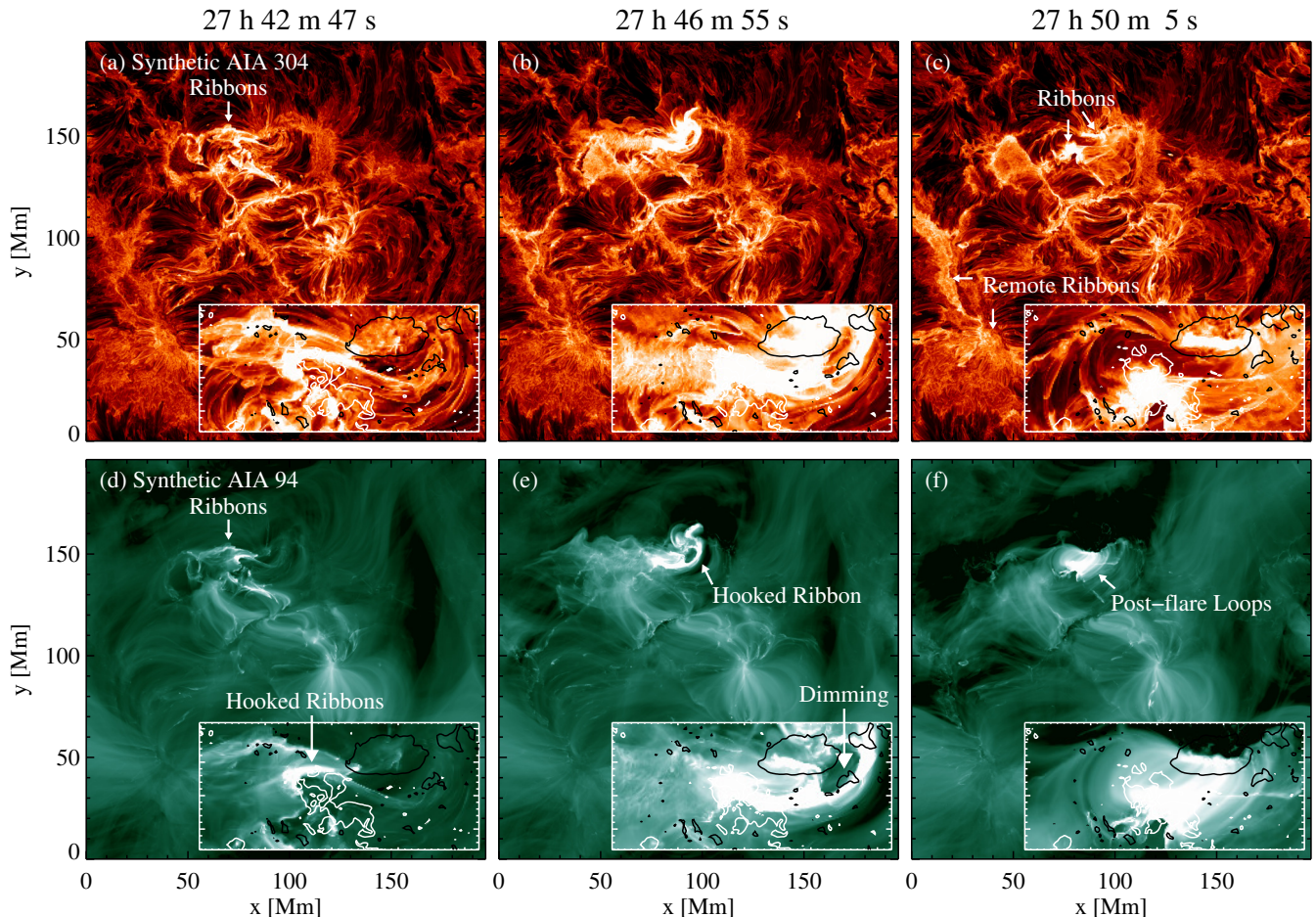
Figure 4. Synthetic AIA 304 Å and 94 Å channel images from the viewpoint at the top of the domain. Large panels show the whole horizontal domain, while the inserts present a zoomed view of the source region of the eruption. Contour lines in the inserts mark $B_z = \pm 1500$ G. Arrows indicate features discussed in the text. An animation that covers the dynamics evolution of about 40 min starting from about 20 min before the flare peak is available in the electronic version.

soft X-ray passbands and give rise to the GOES flux peak.

3.2.2. *Flare Ribbons and Dimmings*

We present in Figure 4 synthetic AIA images in the 304 Å [3] and 94 Å channels from a vertical view. In the three snapshots shown in Figure 4, we highlight a few features in the simulated eruption, which are also commonly seen in observations. An animated version of the figure covers the full course of the eruption.

The first snapshot (left column of Figure 4) captures the very beginning phase of the flare. The insets in each panel shows a zoomed view of the source region with contour lines of $B_z = \pm 1500$ G. A hook-shaped bright rib-

bon can be seen in both 304 Å and 94 Å images, as indicated by the arrows. The ribbon is found to wrap around the positive polarity spot. Meanwhile, a companion ribbon appears almost simultaneously in the negative polarity magnetic-element region north of (larger y) the spot. The evolution shown by the animation demonstrates that the hooked ribbon first appears on the left edge of the positive spot and propagates rightward along the boundary (B_z contour) of the spot. This trend is continued in the next evolution stage as presented below.

The second snapshot shown in the middle column of Figure 4 captures the later development of the flare ribbons in the negative polarity spot region. The right end of the ribbon, which also appears in a hooked shape, does not wrap closely along the boundary of $B_z = -1500$ of the negative spot but reaches two small flux concentrations, as shown more clearly in the insert panels. Meanwhile, we see a formation of a counterpart ribbon

---

[3] Although the interpretation of observations of the 304 Å channel needs to consider the possible blending of coronal emission lines, the synthetic images are based on a temperature response function that captures chromosphere and transition region plasma.

at the southern (smaller y) edge of the negative spot. The evolution of the bright ribbons, which is initiated near $x \approx 60$ Mm and propagates through the PIL, maps the development of reconnection in the coronal magnetic field. This evolution is also consistent with that of the EM along the $y - axis$, as the asymmetric eruption of the flux rope is led by its left end, and the post-flare loops form following the same trend.

A dimming region, which is observed more clearly in the 94 Å image, is formed in the region enclosed by the hooked ribbon and the sunspot. A comparison with Figure 1 and Figure 3 suggests that this dimming region is where the highly sheared horizontal magnetic field anchors and where the apex of the cone-like structure, i.e., one of the footpoints of the flux rope, is rooted.

The third snapshot shown in the right column of Figure 4 highlights the main (post peak) phase of the flare. The 304 Å image shown in Figure 4(c) provides a clear view of the flare ribbons. We find that the ribbon in the negative spot concentrates at the boundary of the coherent spot and that the ribbon in the positive spot appears as a patch that covers the area of the discrete spot. The 94 Å image shows the same flare ribbons, as well as the hot loops connecting them. The temporal evolution shows that the two flare ribbons continuously expand outward for a few minutes after the snapshot shown here, which implies that more magnetic flux is reconnected. It is also interesting to note that new "remote ribbons" are formed on a much larger scale at locations indicated by the arrows in Figure 4(c). The remote ribbons brighten as they extend from $y \approx 100\,Mm$ downward to $y \approx 40$ Mm. This propagation maps the progress of reconnection between the erupting flux rope and the large-scale canopy magnetic field, as shown in the following section.

3.3. *Magnetic Field Involved in the Eruption*
3.3.1. *Large-scale Flux Rope*

In Figure 5, we display the large-scale coronal magnetic field involved in the eruption at four timestamps. The field lines are calculated from seed points, which are randomly distributed in the corona ($z > 15$ Mm) above the region spanning from $x \approx 50$ to 110 Mm and from $y \approx 110$ to 150 Mm. The lines are color coded according to plasma temperatures.

Panel (a) of Figure 5 shows the coronal magnetic field about 20 min before the flare peak. The most evident magnetic structures are a bundle of open field lines connected to a negative spot near the center of the domain and a large-scale magnetic arch connecting the negative spot in the source region of the eruption and positive magnetic concentrations close to the corner of the do-

main. The flux rope is not evident in this large-scale view because the distribution of the seed points is not optimized for capturing it. Nevertheless, it can be found next to the foot point of the large magnetic arch as the bundle of field lines hosting cool plasma.

Panel (b) of Figure 5 captures the magnetic field configuration in the impulsive phase. At this moment, the flux rope erupts and carries cool material into the corona, as indicated by the blue-colored lines, particularly around the axis of the flux rope. The erupting flux rope encounters the overlying arch and pushes the canopy upward. Reconnection between the flux rope and ambient magnetic field is illustrated by red-colored field lines, where the plasma is heated to well over 10^7 K.

Panel (c) of Figure 5 provides the best view of the large-scale flux rope at the flare peak. Moreover, the temperature structure of the flux rope, which is consistent with the EM shown in Figure 3, is clearly illustrated by the colors of the field lines. The cool axis is surrounded by million K plasma, while the hottest plasma wraps at the outermost shell with apparently the largest twist. The hot shell is a consequence of reconnection between the erupted flux rope and the ambient magnetic field, i.e., the open field and large-scale magnetic arch seen in Panels (a) and (b).

Therefore, for the case here, the large-scale flux rope, which is clearly visible and distinguished only when it reaches a sufficient height and size, is an outcome of the expansion of the initial flux rope in the source region and the reconnection of the initial flux rope with the ambient magnetic field. The latter contribution plays a vital role in creating the magnetic and thermal structure of the flux rope we eventually see on large spatial scales.

Panel (d) of Figure 5 shows the magnetic field configuration when the flux rope is about to hit the top boundary. Interestingly, we find that the axis of the flux rope still connects to its original footpoint near the negative polarity spot in the source region, while some of the field lines constituting the shell connect to the negative spot near the center of the domain, which was the foot point of the open field mentioned above.

3.3.2. *Reconnection under the Erupted Flux Rope*

In Figure 6, we zoom into the source region of the initial flux rope. Similar to Figure 5, field lines are calculated from seed points that are fixed in time and randomly distributed over the sunspot pair to capture both flux rope along the PIL and overlying magnetic field lines connecting the two sunspots. Lines are color coded by plasma temperatures as done for Figure 5. An animated version of Figure 6 covers the evolution of the about 25 min.
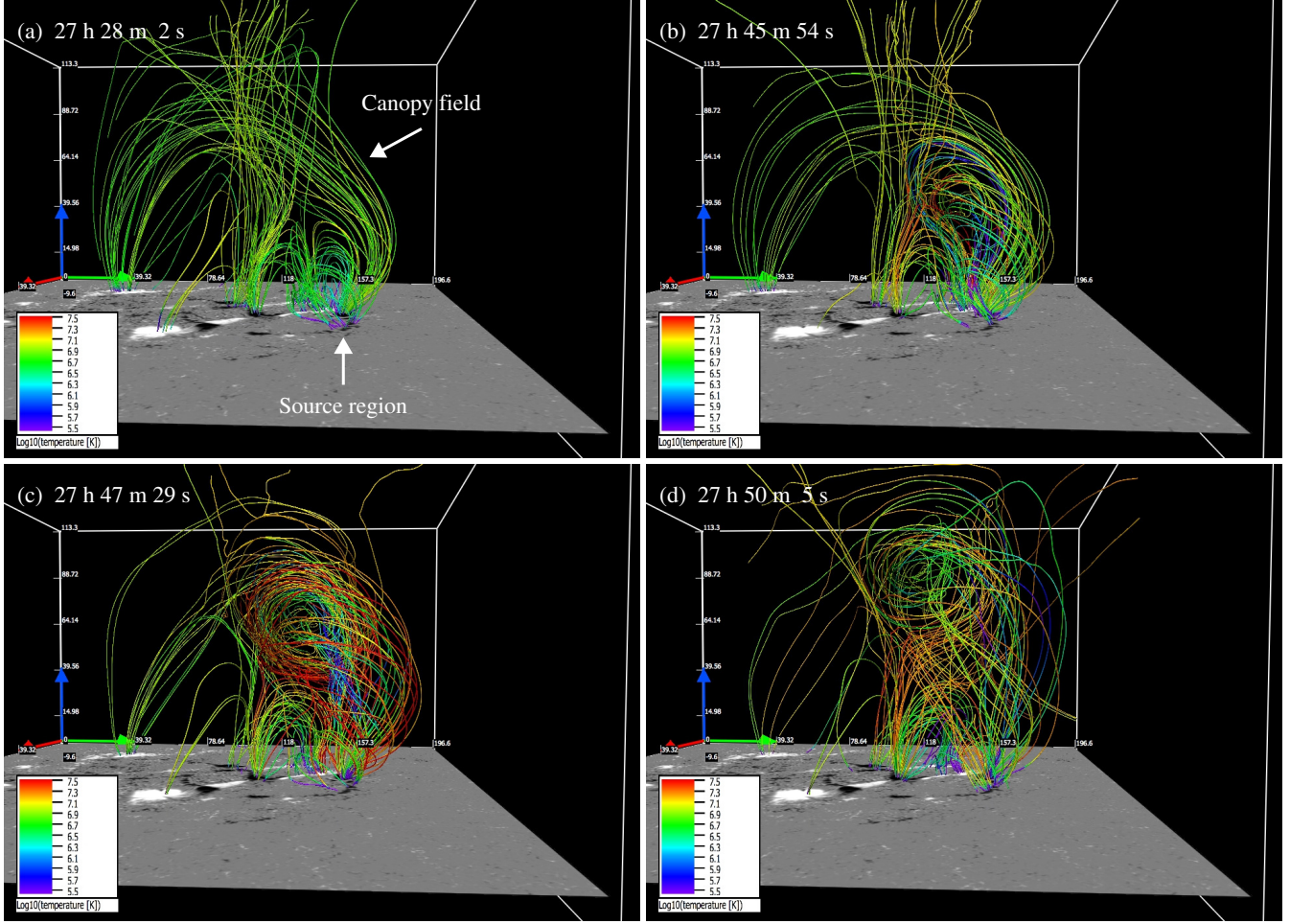
Figure 5. Large-scale magnetic field before and during the eruption. The gray-scale images display B_z at the photosphere. Red, green, & blue arrows indicate the x, y, and z directions, respectively. Colors of the field lines represent plasma temperatures. (a): About 20 min before the flare peak representing the pre-eruption state. (b): Impulsive phase of the flare (about 1.5 min before the flare peak. (c): 9 s seconds after the flare peak. (d): 2.5 min after the peak time. The frame indicates the boundary of the simulation domain.

Panels (a) and (b) of Figure 6 show the magnetic field over this sunspot pair about 20 min before the eruption. The flux rope lies low along the PIL and is filled with plasma cooler than $10^{5.5}$ K. Moreover, a quasi-static rise of the flux rope can be discerned with the upward expansion of the field lines connecting the two sunspots (more clearly shown by the animation).

In Figure 6(c), the flux rope can be clearly identified as a twisted bundle of field lines. Part of the plasma held in the magnetic flux rope has temperatures close to 10 MK, as indicated by the yellow-colored field lines in the flux rope. It also becomes clear that the field lines at the footpoint of the flux rope make a hooked shape and wrap around the negative spot. This corresponds to the bright ribbon that embraces the dimming region as shown in the middle column of Figure 4.

Panel (d) of Figure 6 shows a moment in the impulsive phase, which lies between panels (b) and (c) of Figure 5. The flux rope has erupted and propagated out of the field-of-view for this visualization, leaving only one of its legs, which is highly stretched upright. Panels (e) and (f) of Figure 6 present a clear view of the magnetic reconnection under the erupted flux rope. The field lines connecting the two spots are stretched upward and pushed toward each other. Reconnection is triggered when anti-parallel magnetic fields encounter each other. An elongated current sheet is formed in the layer between the anti-polarity field lines, which is the bright hot thread connecting the erupted flux rope above and the cusp-shaped loops below, as shown in Figure 3(f). A large amount of energy is deposited in the cusp-shaped post-flare loops, where plasma in these loops is heated
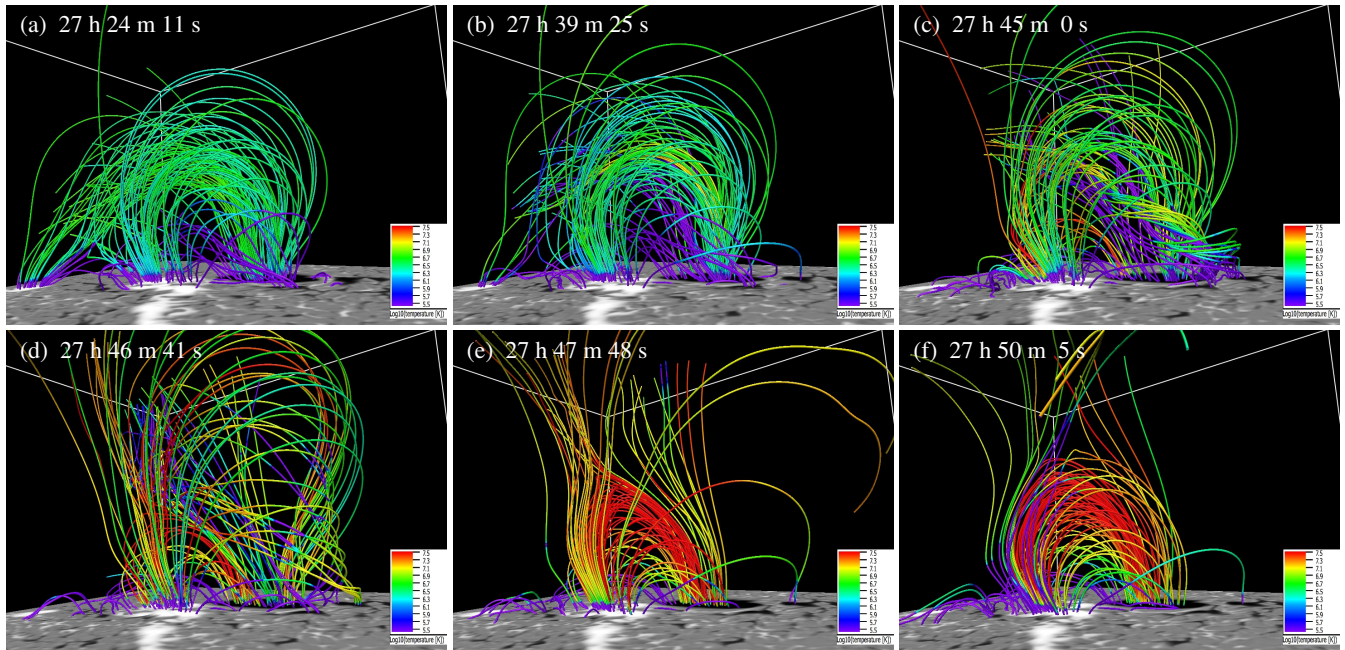
Figure 6. Magnetic field lines above the source region of the eruption. Colors of the field lines represent plasma temperatures. The frame only indicates the boundary of the volume cropped from the whole simulation domain for this visualization. An animated that displays the evolution of about 25 min covered by this figure is available in the electronic version.

to tens of MK and gives rise to the high-temperature observable features seen in Figure 3 and Figure 4.

4. SUMMARY AND DISCUSSION

We present the second part in a series of studies on a radiative MHD simulation of solar active regions, following the first part that presents the general properties of the quiet Sun and non-eruptive stage of active regions Chen et al. (2022). In this study, we focus on the magnetic and emission properties of the largest flare. The results are summarized and discussed as follows.

The flare originates from the eruption of a flux rope along a strongly sheared PIL in a bipole active region. The eruption demonstrates a highly asymmetric shape as one non-active foot point keeps being anchored next to the sunspot, while the other active foot point whips upward. The erupted progenitor flux rope evolves in reconnection with the overlying canopy magnetic field, forming a large scale cone-shaped flux rope. When viewed from the side, the eruption shows a configuration of a multi-thermal flux rope, thin and hot current sheet, and cusp-shaped post-flare loops, which is consistent with classical models and observations. Flare ribbons are generated by a fully self-consistent evolution of plasma thermodynamics properties in response to the disposition of energy in the lower atmosphere.

4.1. Pre-eruption Magnetic Structures

Strongly sheared magnetic fields along PILs (sometimes referred simply as sheared PILs), which imply a strong non-potential magnetic field, have been found for decades (e.g., Heyvaerts et al. 1977; Sun et al. 2012). Whether the pre-eruption magnetic structure is a flux rope or sheared arcades remains a question (Patsourakos et al. 2020). Observations have suggested that flux ropes can form from less twisted configurations (e.g., sheared arcades) on various time scales prior to the eruption (e.g., Wang et al. 2015; James et al. 2017; Chintzoglou et al. 2019). Shortly before the eruption, we see in Figure 2 a flux rope above the photosheric PIL, while beneath the surface, field lines manifest sheared arcades, which implies a close relation between them.

The overlying magnetic field also plays a non-trivial role in solar eruptions. Although the whole domain demonstrates a very complex magnetogram, as shown in Figure 1, the overall large-scale configuration of the magnetic field that is most relevant to this eruption is similar to that considered in the "break out" model Antiochos et al. (1999) and that observed in limb active regions Mason et al. (e.g., 2021). The "break out" model suggests that the reconnection of ambient magnetic fields opens up the confinement above sheared arcades in the source region. A similar process is also seen in the simulation. However, the pre-eruption structure in our simulation is a magnetic flux rope. Thus, it may also be destabilized by, for example, torus instability (Kliem &

Török 2006), depending upon the decay of the overly magnetic field with height.

4.2. *Observational Signatures of Flux Ropes*

Asymmetric eruptions were also reported by, for example, Liu et al. (2009); Joshi et al. (2013); Liu et al. (2015). By comparing EUV observations and a numerical model of Shiota et al. (2005), Tripathi et al. (2006); Li & Zhang (2009) interpreted the one-directional propagation of bright post-flare loops, which is similar to that shown in Figure 4, as an indication of sequential reconnection of the ambient magnetic field triggered by an asymmetric eruption of a flux rope.

When viewed along the x-axis (see Figure 3), the asymmetric geometry of the eruption collapses into a picture that is more similar to classical two-dimensional models (e.g., Shibata et al. 1995) and observations of limb flares triggered by flux rope eruption (e.g., Chen et al. 2020). The plasma that is confined in and affected by the flux rope during the eruption spreads over the whole temperature of the simulation, leading to a multi-thermal flux rope. In observations, although a high-temperature structure was proposed as a proxy of a flux rope (e.g., Zhang et al. 2012), it is now commonly found that flux ropes demonstrate DEMs over a broad temperature range (e.g., Cheng et al. 2012; Hannah & Kontar 2013; Li et al. 2022, and references therein). In particular, we notice a remarkable similarity between the low-temperature EM shown in Figure 3(b) and the AIA 304 Å channel image of flux rope observed on 2011 March 7th (see Fig. 4 of Cheng et al. 2012)[4]

The interaction between an erupting flux rope and overlying magnetic fields is supposed to be universal, although the overlying field may not always be illustrated by EUV loops. In the early phase of the eruption, the overlying field is pushed upward by the flux rope, similar to the process found in observations (Cheng et al. 2011). In the later evolution, the asymmetric flux rope undergoes reconnection with the large-scale overlying canopy field, and the active foot point switches to farther flux concentrations, which marks a clear difference between this eruption and the symmetric configuration considered in most models. In another experiment with the open top boundary[5], the eruption is a more symmetric,

---

[4] The view point of the right column Figure 3 (from positive to negative x) corresponds to observing the structure on the east limb, whereas the observation of Cheng et al. (2012) was on the west limb.

[5] Top boundary is switched to open before the eruption, which changes the magnetic field in the high part of the domain due to increased plasma outflows, while the low-lying progenitor flux rope is not affected.

indicating that the appearance of an eruption is very sensitive to how the erupting flux rope interacts with the overlying field.

4.3. *Observational Signatures of Flares: Hooked Ribbons and Dimmings*

Bright ribbons are a key observable property of solar flares. The flare ribbons of this eruption resemble the hooked flare ribbons that are commonly observed in solar flares (e.g., Janvier et al. 2014; Savcheva et al. 2015; Zhao et al. 2016). In observations, such flare ribbons are interpreted as the imprint of quasi-separatrix layers of the coronal magnetic field where reconnection occurs in the 3D stand flare model. In our simulation, flare ribbons are generated from a self-consistent evolution of plasma thermodynamic properties in response to energy deposition by a strong thermal conductive flux, giving a direct connection between the energy release in the corona and the chromospheric flare ribbons.

Dimming regions embraced by hooked flare ribbons are assumed to be the foot points of erupted flux ropes and hence are used to estimate the axial flux of flux ropes (e.g., Cheng & Ding 2016; Wang et al. 2017; Xing et al. 2020). This assumption can be validated in this simulation, as we see that the dimming corresponds to the root of the flux rope that wraps the sunspot.

Moreover, the fast extension of flare ribbons along both sides of the PIL and the following separation between the flare ribbons reproduce the ribbon evolution commonly observed in flares. Observations by Cheng & Ding (2016) and Qiu & Cheng (2022) noticed that flare ribbons tend to be strongly sheared at the two ends but weakly sheared in the middle. This is consistent with the non-uniform distribution of the shear angle of the magnetic field along the PIL in our simulation.

4.4. *Concluding Remark*

The M2 flare is the strongest flare achieved thus far in radiative MHD simulations that are capable of giving quantitative estimates of flare classes. Although the simulation is not set up to model any particular active region or eruption event, the dynamo-generated magnetic and flow fields provide sufficient realism in the sunspots formed in the photosphere and coronal magnetic field. Therefore, this flare is able to reproduce many key general magnetic and emission features observed in real solar eruptions.

By coupling with a global-scale convective dynamo simulation, this model will help us to trace the origin of solar eruptions back to the solar interior, where the active region magnetic flux is generated and address formation of the flux rope above the photoshere is related

to the sub-surface magnetic and flow fields in the context of flux emergence. Furthermore, the pre-eruption magnetic field exhibits a combination of a pre-existing flux rope within "break out" like canopy field. This raises intriguing questions of whether reconnection or instability acts as the trigger and how these can be differentiated from the observable emission properties.

REFERENCES

Amari, T., Luciani, J. F., Aly, J. J., Mikic, Z., & Linker, J. 2003, ApJ, 585, 1073, doi: 10.1086/345501

Antiochos, S. K., DeVore, C. R., & Klimchuk, J. A. 1999, ApJ, 510, 485, doi: 10.1086/306563

Archontis, V., & Syntelis, P. 2019, Philosophical Transactions of the Royal Society of London Series A, 377, 20180387, doi: 10.1098/rsta.2018.0387

Aulanier, G., Janvier, M., & Schmieder, B. 2012, A&A, 543, A110, doi: 10.1051/0004-6361/201219311

Aulanier, G., Török, T., Démoulin, P., & DeLuca, E. E. 2010, ApJ, 708, 314, doi: 10.1088/0004-637X/708/1/314

Chen, B., Yu, S., Reeves, K. K., & Gary, D. E. 2020, ApJL, 895, L50, doi: 10.3847/2041-8213/ab901a10.48550/arXiv.2005.01900

Chen, F., Rempel, M., & Fan, Y. 2017, ApJ, 846, 149, doi: 10.3847/1538-4357/aa85a0

—. 2022, ApJ, 937, 91, doi: 10.3847/1538-4357/ac8f95

Chen, P. F. 2011, Living Reviews in Solar Physics, 8, 1, doi: 10.12942/lrsp-2011-1

Chen, P. F., & Shibata, K. 2000, ApJ, 545, 524, doi: 10.1086/317803

Cheng, X., & Ding, M. D. 2016, ApJS, 225, 16, doi: 10.3847/0067-0049/225/1/1610.48550/arXiv.1605.04047

Cheng, X., Guo, Y., & Ding, M. 2017, Science China Earth Sciences, 60, 1383, doi: 10.1007/s11430-017-9074-6

Cheng, X., Zhang, J., Liu, Y., & Ding, M. D. 2011, ApJL, 732, L25, doi: 10.1088/2041-8205/732/2/L2510.48550/arXiv.1103.5084

Cheng, X., Zhang, J., Saar, S. H., & Ding, M. D. 2012, ApJ, 761, 62, doi: 10.1088/0004-637X/761/1/6210.48550/arXiv.1210.7287

Cheung, M. C. M., Rempel, M., Chintzoglou, G., et al. 2019, Nature Astronomy, 3, 160, doi: 10.1038/s41550-018-0629-3

Chintzoglou, G., Zhang, J., Cheung, M. C. M., & Kazachenko, M. 2019, ApJ, 871, 67, doi: 10.3847/1538-4357/aaef30

Downs, C., Warmuth, A., Long, D. M., et al. 2021, ApJ, 911, 118, doi: 10.3847/1538-4357/abea78

Fan, Y. 2022, ApJ, 941, 61, doi: 10.3847/1538-4357/aca0ec

Fan, Y., & Fang, F. 2014, ApJ, 789, 35, doi: 10.1088/0004-637X/789/1/35

Fisher, G. H., Canfield, R. C., & McClymont, A. N. 1985, ApJ, 289, 414, doi: 10.1086/162901

Forbes, T. G., & Isenberg, P. A. 1991, ApJ, 373, 294, doi: 10.1086/170051

Georgoulis, M. K., Nindos, A., & Zhang, H. 2019, Philosophical Transactions of the Royal Society of London Series A, 377, 20180094, doi: 10.1098/rsta.2018.0094

Green, L. M., Török, T., Vršnak, B., Manchester, W., & Veronig, A. 2018, SSRv, 214, 46, doi: 10.1007/s11214-017-0462-5

Hannah, I. G., & Kontar, E. P. 2013, A&A, 553, A10, doi: 10.1051/0004-6361/201219727

Heyvaerts, J., Priest, E. R., & Rust, D. M. 1977, ApJ, 216, 123, doi: 10.1086/155453

James, A. W., Green, L. M., Palmerio, E., et al. 2017, SoPh, 292, 71, doi: 10.1007/s11207-017-1093-410.48550/arXiv.1703.10837

Janvier, M., Aulanier, G., Bommier, V., et al. 2014, ApJ, 788, 60, doi: 10.1088/0004-637X/788/1/6010.48550/arXiv.1402.2010

Janvier, M., Aulanier, G., & Démoulin, P. 2015, SoPh, 290, 3425, doi: 10.1007/s11207-015-0710-3

Jiang, C., Feng, X., Liu, R., et al. 2021, Nature Astronomy, 5, 1126, doi: 10.1038/s41550-021-01414-z

Jin, M., Manchester, W. B., van der Holst, B., et al. 2017, ApJ, 834, 172, doi: 10.3847/1538-4357/834/2/172

Joshi, N. C., Srivastava, A. K., Filippov, B., et al. 2013, ApJ, 771, 65, doi: 10.1088/0004-637X/771/1/65

Kliem, B., & Török, T. 2006, PhRvL, 96, 255002, doi: 10.1103/PhysRevLett.96.255002

Kowalski, A. F., Allred, J. C., Daw, A., Cauzzi, G., & Carlsson, M. 2017, ApJ, 836, 12, doi: 10.3847/1538-4357/836/1/12

Kusano, K., Bamba, Y., Yamamoto, T. T., et al. 2012, ApJ, 760, 31, doi: 10.1088/0004-637X/760/1/31

Li, L., Song, H., Peter, H., & Chitta, L. P. 2022, ApJL, 941, L1, doi: 10.3847/2041-8213/aca47b10.48550/arXiv.2211.11148

Li, L., & Zhang, J. 2009, ApJ, 690, 347, doi: 10.1088/0004-637X/690/1/347

Li, S., Jaroszynski, S., Pearse, S., Orf, L., & Clyne, J. 2019, Atmosphere, 10, doi: 10.3390/atmos10090488

Lin, J., & Forbes, T. G. 2000, J. Geophys. Res., 105, 2375, doi: 10.1029/1999JA900477

Liu, C., Deng, N., Liu, R., et al. 2015, ApJL, 812, L19, doi: 10.1088/2041-8205/812/2/L19

Liu, R., Alexander, D., & Gilbert, H. R. 2009, ApJ, 691, 1079, doi: 10.1088/0004-637X/691/2/1079

Mason, E. I., Antiochos, S. K., & Vourlidas, A. 2021, ApJL, 914, L8, doi: 10.3847/2041-8213/ac0259

Moore, R. L., Sterling, A. C., Hudson, H. S., & Lemen, J. R. 2001, ApJ, 552, 833, doi: 10.1086/320559

Patsourakos, S., Vourlidas, A., Török, T., et al. 2020, SSRv, 216, 131, doi: 10.1007/s11214-020-00757-910.48550/arXiv.2010.10186

Priest, E. R., & Forbes, T. G. 2002, A&A Rv, 10, 313, doi: 10.1007/s001590100013

Qiu, J., & Cheng, J. 2022, SoPh, 297, 80, doi: 10.1007/s11207-022-02003-710.48550/arXiv.2205.03004

Rempel, M. 2017, ApJ, 834, 10, doi: 10.3847/1538-4357/834/1/10

Savcheva, A., Pariat, E., McKillop, S., et al. 2015, ApJ, 810, 96, doi: 10.1088/0004-637X/810/2/96

Shibata, K., & Magara, T. 2011, Living Reviews in Solar Physics, 8, 6, doi: 10.12942/lrsp-2011-6

Shibata, K., Masuda, S., Shimojo, M., et al. 1995, ApJL, 451, L83, doi: 10.1086/309688

Shiota, D., Isobe, H., Chen, P. F., et al. 2005, ApJ, 634, 663, doi: 10.1086/496943

Sun, X., Hoeksema, J. T., Liu, Y., et al. 2012, ApJ, 748, 77, doi: 10.1088/0004-637X/748/2/77

Török, T., Kliem, B., & Titov, V. S. 2004, A&A, 413, L27, doi: 10.1051/0004-6361:20031691

Tripathi, D., Isobe, H., & Mason, H. E. 2006, A&A, 453, 1111, doi: 10.1051/0004-6361:20064993

Wang, H., Cao, W., Liu, C., et al. 2015, Nature Communications, 6, 7008, doi: 10.1038/ncomms8008

Wang, W., Liu, R., Wang, Y., et al. 2017, Nature Communications, 8, 1330, doi: 10.1038/s41467-017-01207-x

Wyper, P. F., Antiochos, S. K., & DeVore, C. R. 2017, Nature, 544, 452, doi: 10.1038/nature22050

Xing, C., Cheng, X., & Ding, M. D. 2020, The Innovation, 1, 100059, doi: 10.1016/j.xinn.2020.10005910.48550/arXiv.2011.10750

Zhang, J., Cheng, X., & Ding, M.-D. 2012, Nature Communications, 3, 747, doi: 10.1038/ncomms1753

Zhao, J., Gilchrist, S. A., Aulanier, G., et al. 2016, ApJ, 823, 62, doi: 10.3847/0004-637X/823/1/62